Pushing the Limits of LiDAR: Accurate Performance Analysis of Indoor 3D LiDARs

Xiting Zhao Sören Schwertfeger
ShanghaiTech University, Key Laboratory of Intelligent Perception and Human-Machine Collaboration – ShanghaiTech University, Ministry of Education, China
{zhaoxt, soerensch}@shanghaitech.edu.cn

Abstract

Light Detection and Ranging (LiDAR) technology has become crucial in robotics and autonomous systems for generating precise 3D environmental representations. However, challenges persist in achieving high accuracy and precision, especially in indoor environments. This paper rigorously analyzes the performance of various indoor LiDAR systems under different conditions. We present a novel experimental methodology, which quantifies LiDAR accuracy and precision, examining factors such as sensor type, environmental conditions, and target characteristics. Using an extensive dataset collected from nine distinct locations with more than 36000 LiDAR scans, combined with high-precision reference data from a FARO laser scanner, our analysis reveals significant insights into the accuracy and precision across different LiDAR models. The resulting public dataset, which include detailed point clouds and groundtruth labels, are expected to serve as a valuable resource for developing and validating advanced LiDAR processing techniques and benchmarks for various applications. The dataset will be publicly available at http://lidaraccuracy.github.io.

1. Introduction

Rapid advancements in Light Detection and Ranging (LiDAR) technology have significantly impacted robotics and autonomous driving, establishing it as an essential tool for precise environmental mapping and navigation. The ability of LiDAR to generate high-resolution 3D representations is indispensable for applications like autonomous vehicles, drones, and mobile robots that require accurate perception and real-time mapping [24]. The integration of LiDAR into Simultaneous Localization and Mapping (SLAM) algorithms has substantially improved navigation systems, especially in indoor environments where GPS is unavailable. In robotics, LiDAR's capabilities facilitate efficient environmental perception, obstacle avoidance, and object interaction, while in autonomous vehicles, it plays a critical role in obstacle detection and safe navigation. Beyond robotics, LiDAR's utility extends to geospatial analysis, urban planning, and environmental monitoring, underscoring its extensive relevance across various domains.

Despite the significant improvements in LiDAR technology over recent years, challenges related to the precision and accuracy of LiDAR data persist. Precision refers to the consistency of measurement results, while accuracy denotes the closeness of these results to the true value. Although modern LiDAR systems have seen enhancements in both aspects, there remains a gap when compared to high-end Terrestrial Laser Scanners (TLS), which offer mm-level accuracy but are often less practical for dynamic and mobile applications due to their size, cost, and operational complexity [26].

The accuracy and precision of LiDAR measurements directly impact the reliability and effectiveness of systems relying on them. In robotics, precise spatial information is essential for tasks such as autonomous navigation, obstacle avoidance, and interaction with objects. High accuracy in LiDAR data ensures that robots can operate safely and efficiently in complex environments, reducing the risk of collisions and improving task performance. Similarly, in autonomous vehicles, accurate LiDAR data is vital for ensuring safe and reliable navigation, enabling vehicles to detect and identify objects, pedestrians, and road conditions with high fidelity.

LiDAR measurements are influenced by a complex interplay of factors, particularly in indoor environments. These factors include both intrinsic characteristics of the LiDAR systems and extrinsic environmental conditions [16]. The inherent properties of LiDAR devices, such as their hardware design, number of channels, and field of view, fundamentally affect their performance in terms of range, resolution, and accuracy. Concurrently, measurement accuracy is heavily impacted by environmental variables, including incident angle, distance to target, surface reflectivity, and material properties. The intricacies of indoor spaces, characterized by reflective surfaces, variable lighting conditions, and complex geometries, introduce additional complexity.

Assessing and quantifying the precision and accuracy of LiDAR systems is essential for enhancing a wide range of applications. In traditional measurement and reconstruction tasks, improvements in LiDAR accuracy can yield more detailed and reliable 3D models of environments, which are crucial for both practical and research purposes. It also holds the potential to advance cutting-edge computer vision and robotics algorithms. For example, in Truncated Signed Distance Function (TSDF) based mapping approaches[19], the precision of LiDAR points contributes to more accurate surface thickness estimations, thereby enhancing the fidelity of 3D reconstructions. Similarly, in the emerging field of 3D Gaussian Splatting[15], which seeks to represent 3D scenes as collections of 3D Gaussians, knowing the precision and accuracy of LiDAR points may improve the estimation of Gaussian distributions, offering a more reliable alternative to traditional Structure from Motion (SfM) techniques.

This study aims to push the limits of LiDAR performance in indoor settings. Our main contributions are as follows:

- A highly accurate experimental methodology for LiDAR performance analysis using precision reference data.
- Quantitative analysis of LiDAR accuracy and precision dependencies on key factors such as incident angle, distance, and material properties.
- Comprehensive performance comparison of multiple modern LiDAR models under diverse indoor conditions.
- A large-scale public dataset of over 36,000 LiDAR scans with high-precision ground truth and extensive metadata to support further research and development.

The paper is structured as follows: Section 2 provides an overview of related work in LiDAR accuracy assessment and calibration. Section 3 details our experimental setup and data collection hardware. Section 4 presents the collection of our dataset and evaluation metrics. Section 5 offers a comprehensive analysis of the dataset results, including detailed error assessments across various parameters. Section 6 verifies our findings. Finally, Section 7 concludes the paper and suggests directions for future research.

2. Related Work

A line of research focuses on the calibration of LiDAR sensors. Early studies mainly focused on older rotating LiDAR models such as the Velodyne. For instance, Muhammad et al.[20] devised a calibration method for the Velodyne HDL64E, using a controlled environment and multiple scans. Nouira et al.[21] introduced a target-free calibration technique for the HDL32E requiring high-resolution point clouds. Bergelt et al.[3] and Sun et al.[25] proposed intrinsic calibration techniques that assume minimal initial errors or fixed sensor positions—assumptions that may not be universally applicable. Atanacio-Jiménez et al.[2] used specific pattern planes for the calibration of the HDL-64E. While these studies have significantly advanced the LiDAR calibration, they primarily focus on older models characterized by more complex structures and higher error margins. Modern LiDAR sensors, with their different designs and reduced error margins, may therefore require further research to develop more general calibration approaches.

In parallel, self-calibration of 3D LiDAR systems has become a critical research topic. Lee et al.[18] explored the validation of LiDAR calibration using simulators, though such approaches may not fully capture the complexities of real-world error sources. Agishev et al.[1] proposed a self-supervised depth correction method utilizing a total station and Leica scanner, which demonstrated the influence of incidence angles on measurements. However, this method has limitations, as it applies to only one specific type of LiDAR, and the platform can only move horizontally, without accounting for varied rotational scenarios.

Another area of research is the accuracy assessment and performance analysis of different LiDAR scanners. Kelly et al.[14] evaluated the distance measurement accuracy of the Velodyne HDL32E and Livox Mid40, identifying temporal biases in both devices. Similarly, Glennie and Hartzell[7] conducted a detailed geometric accuracy analysis of the Ouster OS1-64 and Livox Mid40. These studies used Rigel 3D scanners for precise point cloud acquisition, but did not have precise sensor poses, instead estimating them through target or plane matching. Cattini et al.[4] presented a procedure for characterizing and comparing 3D LiDAR systems, but their analysis did not fully explore the limitations and applicability of different LiDAR models across diverse scenarios. Laconte et al.[16] investigated the relationship between measurement noise and incidence angles, revealing significant biases at high incidence angles for several LiDAR models. However, these approaches, which measure sensor translation via tracks and use specific materials, do not incorporate varied rotations or offer a ground truth point cloud analysis in typical environments.

In other applications like automotive, Haider et al.[8] and Lambert et al.[17] evaluated the performance of MEMS-based and other common 3D LiDARs. However, these studies often focused on specific targets, like balls or chessboards, within controlled environments, may limit their relevance to diverse real-world conditions, particularly in indoor settings. Pathak et al.[23] presented a new technique for the update of a probabilistic spatial occupancy grid map using a 3D forward sensor model. Elaksher et al. [5] also offered a quantitative assessment of LiDAR data accuracy, focusing on outdoor UAV applications.

LiDAR	Channels	Resolution	FOV	Range	Accuracy(cm)	Precision(cm)
Hesai PandarQT64[9]	64	600	104.2°	20	±3	2
Hesai PandarXT32[10]	32	2000	31°	50	±2, up to ±1	2, up to 0.5
Ouster OS0-128 Rev6[11]	128	1024	90°	15	±3 lambertian ±10 retroreflectors	±2(0.3-1m) ±1(1-10m) ±1.5(10-15m) ±5(>15m)
Ouster OS0-128 Rev7[12]	128	1024	90°	35	±2.5 lambertian ±5 retroreflectors	0.8-4cm Increase w/ dist.

Table 1. LiDAR Device Specifications (From Manufacturer Datasheets) Range means the max detectable distance at 10% Reflectivity.

3. Data Collection and Calibration

3.1. LiDAR Hardware

The study evaluates the accuracy of four commonly used LiDAR sensors in indoor applications. Table 1 summarizes their key specifications. The selection of these sensors was motivated by their popularity and representativeness of common indoor LiDAR solutions.

- Hesai PandarQT64 (HesaiQT): Emphasizing low cost, compact size, lightweight design, and a wide field of view, it is suitable for applications requiring extensive coverage and efficient mapping in larger spaces [9].
- Hesai PandarXT32 (HesaiXT): Despite having fewer channels, it focuses on high precision and longer detection range [10].
- Ouster OS0-128 Rev6 (Ouster6): Offering high angular resolution and point cloud density in a compact form factor, it can capture millions of points per second for detailed environmental mapping [11].
- Ouster OS0-128 Rev7 (Ouster7): Powered by the next-generation L3 chip, this upgraded sensor delivers double the range, enhanced object detection, increased precision and accuracy, and greater reliability [12].

3.2. Data Collection Hardware

3.2.1 FARO Laser Scanner

A FARO Focus X330 terrestrial laser scanner was employed to establish highly accurate ground truth reference data. Renowned for its precision, with a ranging error of ±2 mm and ranging noise of less than 0.5 mm, it ensures minimal systematic bias and high precision in the reference point clouds [6]. The scanner's extensive field of view of 300°x360° offers comprehensive coverage of the test environment, and its high resolution ensures detailed representation of object shapes and surface textures. The superior accuracy of the FARO allows any observed errors in the LiDAR data to be attributed to the LiDAR sensors themselves rather than the limitations of the ground truth. The FARO Focus X330 was calibrated by the manufacturer and its accuracy is verified.

3.2.2 OptiTrack Tracking System

The OptiTrack motion capture system, comprising 12 ”Prime 13” high-precision cameras, was employed to track the marker with a translation accuracy of sub-millimeter [22]. By creating a rigid body with multiple markers, the rotation can be tracked precisely. It ensures precise LiDAR localization by providing accurate data on the LiDAR's pose, which is essential for transforming the captured point clouds into the ground truth coordinate system. The sub-millimeter accuracy of the OptiTrack system minimizes uncertainties in the LiDAR-to-arm calibration process, enabling the isolation of errors from the LiDAR sensors instead of pose.

3.2.3 Robot Platform with Arm and LiDAR mount

As shown in Figure 1a, the Clearpath Husky mobile robot served as a stable base for the LiDAR sensors. Its robust construction effectively minimized vibrations and unwanted motion during data collection, providing the necessary stability for accurate data acquisition.

A Schunk LWA 4P robotic arm was mounted on the Husky using a CNC aluminum frame to precisely position the LiDAR sensors for systematic testing. The arm's 6DOF motion allowed for flexible placement of the LiDAR, enabling the investigation of their accuracy under various scenarios with different distances and angles of incidence.

The LiDAR sensor was installed using a high-precision, temperature-resistant mount fabricated from photopolymer resin via 3D printing. The mount was firmly attached to the arm's end effector, with eight OptiTrack markers creating a rigid body for it. The screw holes were designed according to each LiDAR's manual, and the axis was aligned. The 3D printer had a nominal error of 0.2mm, verified by measurement.

3.3. Test Environment and Data Collection

The test environment, as shown in Figure 1c, was designed to include a wide range of materials such as wood, paper, multi-colored plastic sheets, foam, wallpaper, electrostatic stickers, whiteboards, curtains, cabinets, floors, and ceilings, among others. This inclusive setup comprised 28 dis-

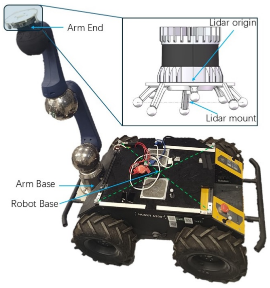

(a) Robot platform with Arm and LiDAR mounting

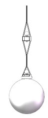

(b) Calibration Target

(c) FARO Panorama Image of Test Environment with 5 Calibration Targets

Figure 1. Experimental Setup and Equipment

tinct categories, with careful consideration to minimize potential interference from glass [27].

For comprehensive and robust data collection, a FARO scanner was used to gather high-precision ground truth data at 10 distinct locations. Additionally, the LiDAR data were acquired at 9 locations using a robotic platform. At each robotic location, the arm was programmed to adopt 10 random poses, holding each pose for 10 seconds to capture LiDAR data. These random poses were chosen to sample a variety of viewing angles and distances for each sensor at each location. This generated an extensive dataset, with 100 LiDAR scans per pose and a total of 90 poses for each LiDAR sensor. This rich dataset enables a thorough analysis of the sensors' performance under various conditions, enhancing our understanding of their capabilities and limitations.

3.4. Calibration

From	To	Pose
Robot Base	Opti	Opti marker (CAD)
Robot Base	Arm Base	CAD
Arm Base	Arm End	URDF
LiDAR Mount	Arm End	CAD
LiDAR mount	Opti	Opti marker (CAD)
LiDAR origin	LiDAR mount	CAD & Datasheet
FARO	FARO Sphere	FARO Scene
FARO Sphere	Opti	Opti marker ICP

Table 2. Calibration Chain for LiDAR Position Determination

To accurately evaluate the accuracy and precision of the LiDAR system, it is critical to determine its precise pose within the FARO ground-truth point cloud. This calibration process is essential for ensuring that the measurements are reliable and can be effectively compared against the ground-truth data. Table 2 summarizes the calibration chain used in our experimental setup. The following subsections describe the methods and processes used to achieve this calibration.

3.4.1 Pose from Robotic Arm and OptiTrack

The first method we used to determine the LiDAR's position involves a robotic arm and OptiTrack markers fixed on the robot's chassis. The end-effector pose of the robotic arm is combined with the OptiTrack measurements to calculate the LiDAR's position. This approach can reduce the impact of potential occlusions that interfere with the OptiTrack's visibility when the LiDAR rotates at various angles.

To get the arm pose, we use the ROS driver and the URDF of the arm. However, there's an error in the existing URDF of the robotic arm, so we re-calibrated the arm's length. This involved rotating each axis to form a circle and fitting the radius of the circle using the pose of the OptiTrack marker to calculate the arm length accurately. By this calibration, exact dimensions of the robotic arm were established, and we use the new length for the URDF.

The transformation from the robotic arm's end-effector to the LiDAR mount and the robot base OptiTrack rigid body to arm base was determined using CAD data and verified by measurement.

3.4.2 Pose directly from OptiTrack

In the second method, we directly used the OptiTrack system to determine the position of the LiDAR mount. This provides an independent way to verify the LiDAR's location, which is crucial for cross-validation. By obtaining the position of the LiDAR mount directly from the OptiTrack system, we can compare it with the position obtained through the robotic arm-based method.

3.4.3 LiDAR Mount to LiDAR Origin

The transformation from the LiDAR mount to the LiDAR origin was calculated using CAD data and the LiDAR's datasheet. This transformation is essential for accurately relating the LiDAR's pose to its sensor origin, which is the reference point for all LiDAR measurements.

3.4.4 FARO and OptiTrack Calibration

Establishing an accurate transformation between the FARO laser scanner and the OptiTrack tracking system was crucial for aligning LiDAR measurements with the ground truth reference. Shown in Figure 1b, a custom calibration target was designed and 3D printed, incorporating two OptiTrack markers and one FARO registration sphere. This target was suspended vertically using a ring to ensure consistent orientation relative to gravity, simplifying vertical alignment.

The calibration procedure involved placing five targets at distinct locations in the environment. To reduce errors, we collected two FARO scans and averaged the OptiTrack markers positions. The 3D offset of the FARO sphere center relative to the bottom OptiTrack markers was determined through precise CAD design of the calibration target. The FARO registration spheres' center was fitted by the FARO SCENE software. Since we have two OptiTrack markers vertically, we can get the gravity direction and get the FARO spheres' center accordingly from the lower OptiTrack markers. The Iterative Closest Point (ICP) algorithm was employed to align corresponding point sets in the FARO and OptiTrack data, yielding precise transformations (rotation and translation) between the two coordinate systems. After the ICP, final average point-to-point distance between FARO and OptiTrack markers was 2.024 mm, verifying the accuracy of calibration.

4. Dataset and Experiment

Our study has produced a comprehensive dataset that encompasses a wide range of LiDAR measurements under diverse conditions. This dataset includes over 36000 scans from four LiDAR models with more than 2.8 billion points, along with high-precision ground truth data from aligned FARO scans. It is enriched with detailed calibration information, precise pose data, and extensive metadata for each point in the LiDAR scans, providing a solid foundation for various research applications in the field of 3D sensing and robotics. While the dataset currently features data from one primary indoor scene to ensure consistent evaluation, data from nine distinct locations is available.

4.1. Evaluation Metrics

To quantify the accuracy and performance of LiDAR systems, we defined specific evaluation metrics to assess how well the sensors capture accurate distance measurements and maintain consistency.

We define D_i as individual measured distances in one direction, D_{true} as the true distance to the target, $\bar{D}$ as the mean of measured distances, and N as the total number of measurements.

Range Accuracy is the average difference between measurements and the true distance, as measured by a single direction:

$$\text{Range Accuracy} = \frac{1}{N}\sum_{i=1}^{N} |D_i - D_{\text{true}}|$$

Range Precision is the standard deviation of multiple measurements taken by a single direction:

$$\text{Range Precision} = \sqrt{\frac{1}{N}\sum_{i=1}^{N} \left(D_i - \bar{D}\right)^2}$$

Lower values in both metrics indicate better performance, with accuracy reflecting closeness to true distance and precision indicating measurement consistency.

4.2. Generation of Ground Truth Data

The generation of ground truth data is a crucial step in evaluating the accuracy and performance of LiDAR systems. In this study, we employed the FARO scanner to capture ten scene scans and two calibration scans, which were subsequently aligned using FARO Scene software with a maximum point error of 1.5mm. The aligned scans were then manually cleaned using CloudCompare, and Poisson reconstruction[13] was applied to generate a high-quality mesh. Then Agisoft software was utilized to create color and FARO intensity textures for the mesh, and 28 object categories were manually annotated on the texture, resulting in a labeled ground truth mesh.

The ground truth mesh was transformed into the OptiTrack coordinate system using calibrated transformation matrices. Poses from OptiTrack and the arm were also transformed to LiDAR coordinate system. To further mitigate potential errors, we computed average poses for stationary LiDAR positions, thereby enhancing the overall accuracy of our ground truth pose.

4.3. Data Processing

We extracted point clouds from raw LiDAR data using ROS drivers, obtaining x, y, z, intensity values, ring numbers, and indices within each ring for each point. We transformed these point clouds to the OptiTrack coordinate system for alignment with our ground truth mesh.

Using point clouds from each static LiDAR position, we performed ray casting on the ground truth mesh using Open3D[28]. This allowed us to compute accuracy and precision metrics for each point. We also extracted metadata including incident angle, FARO intensity, label information, and distance from the ray casting. This comprehensive dataset, combining raw measurements and derived metrics, formed the basis for our analysis of LiDAR performance across various conditions and configurations.

4.4. Pose Evaluation

4.4.1 OptiTrack and Arm Pose Cross-Validation

In Table 3, we assessed the pose estimation accuracy derived from both the robotic arm and the OptiTrack system by calculating their Euclidean distance. This analysis unveiled that all LiDAR poses exhibited low static errors, ranging from 4.9mm to 5.8mm. However, when including dynamic movements, the errors increased slightly. This might be due to there are minor errors in the arm position and time synchronization. Through cross-validation, it was found that the difference in pose estimation was only a few millimeters at the overall scale of several meters, which further demonstrates the correctness of the calibrated pose.

Error	HesaiQT	HesaiXT	Ouster6	Ouster7
All	7.06	7.3	9.1	10.5
Static	5.5	4.9	5.0	5.8

Table 3. OptiTrack and Arm Pose Distance (mm)

4.4.2 Thickness of the Plane Evaluation

To further validate our calibration, we analyzed the plane thickness. Two distinct planes, one made of wood and the other from a metal cabinet, were selected. We extracted the points corresponding to each plane from the point clouds and utilized the RANSAC algorithm to fit the plane. The standard deviation of the point-to-plane distances was then calculated to assess the thickness of the planes. This evaluation was carried out across four different point cloud configurations, as detailed in Table 4. The ”Static” refers to single static pose, while the ”Opti” and ”Arm” represent one robot position with 10 different arm poses. The ”All Opti” encompasses pointclouds from nine different robot positions with all LiDAR poses.

Our results suggest that poses from the arm lead to a greater plane thickness, indicating that Opti poses are more accurate. The slight increase in the plane thickness of the ”Opti” compared to the static point cloud can be attributed to variations in the incident angle and distance due to different viewpoints.

Point-Plane	Sensors	Static	Opti	Arm	All opti
Plane1 Wood	HesaiQT	10.3	10.7	12.2	11.7
	HesaiXT	4.4	5.0	6.7	7.6
	Ouster6	6.7	10.9	12.8	11.0
	Ouster7	4.9	6.3	7.7	10.4
Plane2 Metal	HesaiQT	7.4	10.1	12.9	12.7
	HesaiXT	3.1	6.4	8.2	9.3
	Ouster6	6.8	9.9	9.8	12.6
	Ouster7	5.1	7.3	11.8	9.7

Table 4. Std. of the Point-Plane Distance (mm)

4.4.3 Pointcloud to Mesh Distance Evaluation

To assess the overall accuracy, we measured the distance between the fused point cloud and ground truth mesh from FARO scanner. The results in Table 5 demonstrate that, with the exception of Ouster6, which exhibited a slight bias in accuracy, the mean cloud to mesh distances for the other LiDAR sensors are quite low, indicating a good Opti to FARO calibration and highly accurate poses. FARO pointcloud itself also aligns well with the mesh.

Dist	FARO	HesaiQT	HesaiXT	Ouster6	Ouster7
Mean	0.2	3.0	0.5	25.0	6.6
Std	0.8	24.2	18.6	28.4	21.1

Table 5. Cloud to Mesh distance (mm)

5. Dataset Analysis

A detailed analysis of the dataset is conducted, concentrating on the factors that significantly influence the precision and accuracy of the LiDAR sensors. Due to space constraints, we have selected key figures to highlight these impacts, additional figures and calibration board analysis are provided in the Appendix.

5.1. Histogram

A histogram analysis was performed to visualize the distribution of the LiDAR data.

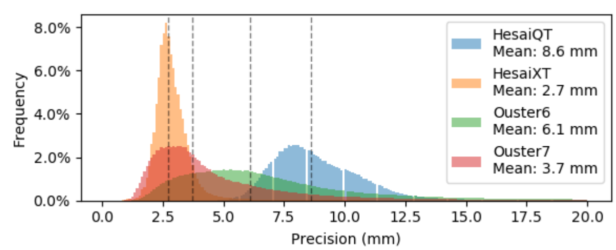

Figure 2. Precision Histogram

Figure 2 illustrates the distribution of precision measurements for four LiDAR models. HesaiXT shows the highest peak, indicating a strong concentration of highly precise measurements. Ouster7 also demonstrates a substantial level of precision, though its distribution is broader compared to HesaiXT. Ouster6 and HesaiQT exhibit a wider spread in precision values, with peaks further to the right, suggesting lower overall precision compared to other LiDARs.

Figure 3 illustrates the distribution of accuracy measurements for four LiDAR models. Among these, HesaiXT exhibits the highest accuracy, with a peak precisely centered at zero, indicating minimal error. In contrast, the accuracy distribution for Ouster6 shows a noticeable deviation from zero, suggesting a systematic bias or lower accuracy. Similarly, Ouster7 also indicates a minor deviation from zero accuracy, performing better than Ouster6.

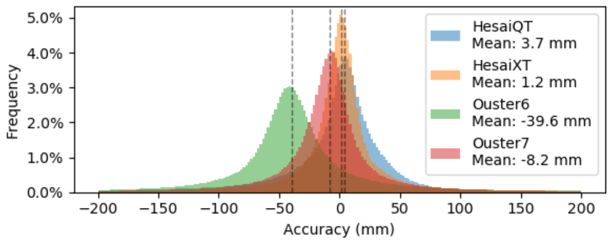

Figure 3. Accuracy Histogram

5.2. Error Analysis Regarding Incident Angle

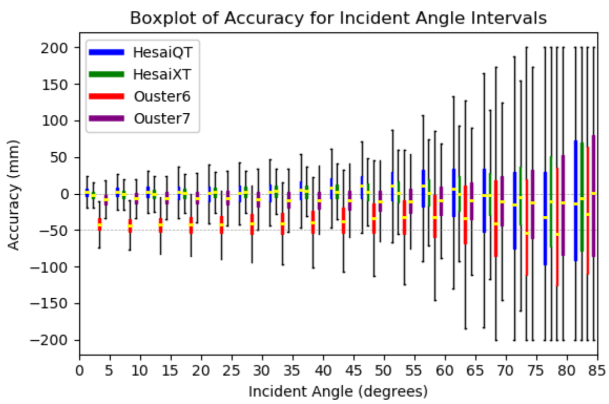

Figure 4. Incident Angle vs Accuracy

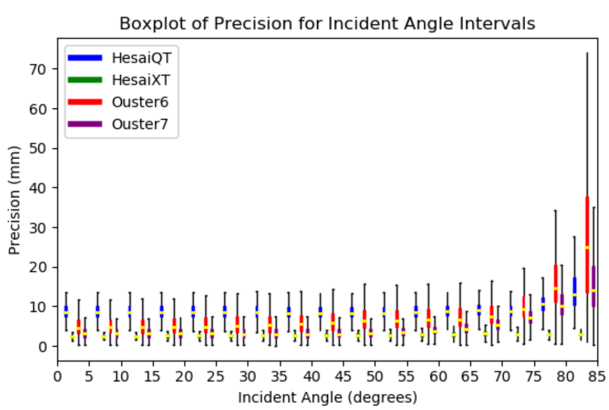

Figure 5. Incident Angle vs Precision

Incident angle has a significant impact on the accuracy and precision of LiDAR measurements. Figure 4 shows the decline in measurement accuracy with increasing incident angle. Similarly, Figure 5 highlights the reduction in precision under the same conditions. Figure 6 demonstrates the corresponding decrease in intensity as the incident angle increases. These findings underscore the importance of considering incident angle in LiDAR calibration and data interpretation. The data reveal a clear trend: as the incident

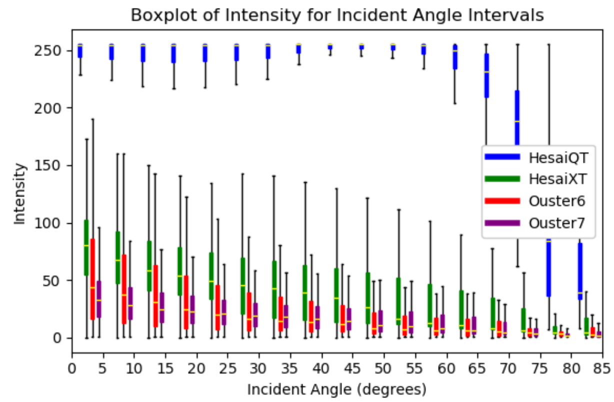

Figure 6. Incident Angle vs Intensity

angle exceeds approximately 70 degrees, both accuracy and precision degrade significantly.

5.3. Error Analysis Regarding the Distance

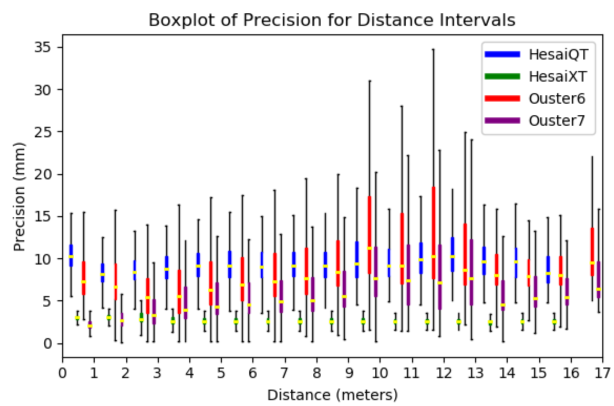

Figure 7. Distance vs Precision

We examine how the distance affects the precision of the LiDAR sensors. As shown in Figure 7, the precision of both Ouster LiDARs decreases as the distance increases. This trend aligns with the description in their datasheet. In contrast, two Hesai LiDARs show no significant change in precision with increasing distance, indicating a more stable performance over varying distances.

5.4. Error Analysis Regarding Different Materials

The impact of various materials on LiDAR measurements was also analyzed. Figure 8 shows that different labels representing distinct material surfaces have varying precision and intensity. Notably, materials with lower FARO intensity also tend to have lower LiDAR intensity. These materials with lower intensity show a decrease in precision, highlighting the sensitivity of LiDAR to material properties. This analysis emphasizes the importance of considering material-specific responses when interpreting LiDAR data in diverse environments.

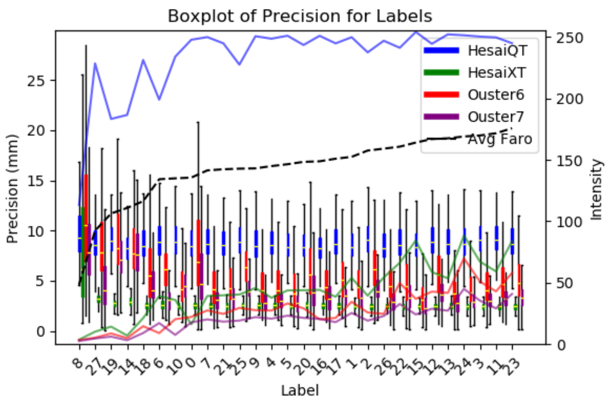

Figure 8. Label vs Precision/ Intensity

5.5. Error Analysis Regarding the Ring Number

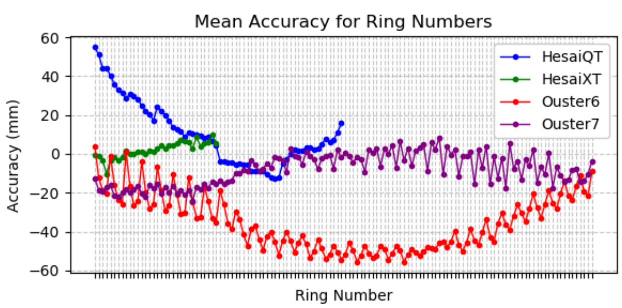

Figure 9. Ring Number vs Accuracy

We conducted an analysis of LiDAR accuracy with respect to the ring number. To minimize the influence of other factors, we selected high-reflectivity labels, limited the incident angle to within 70 degrees, and chose distances ranging from 1.5 to 6 meters. Figure 9 reveals that both the HesaiQT and Ouster sensors exhibit centimeter-level errors with different rings. Notably, the Ouster LiDARs show significant variations in accuracy across different rings, following a discernible pattern that may be linked to the sensor's inherent characteristics. Similarly, the HesaiQT LiDAR is also notably affected by the ring number, indicating that this factor is crucial for the overall performance of these sensors.

6. Result Verification

To validate our findings, we focused on Ouster6, the sensor with the largest observed error. We tested two approaches. Both involved filtering the points with a large incident angle and low intensity. The first one was to then apply a uniform mean accuracy offset across all rings. The second one was to calculate and apply individual offsets to each ring. As shown in Table 6, calculating the distance from the point cloud to the mesh after applying either method resulted in a reduction in both the average and standard deviation of errors. However, the approach utilizing individual ring offsets achieved marginally superior results.

Dist	Origin	Offset	Ring
Mean	25.0	3.19	0.80
Std	28.4	26.9	26.1

Table 6. Cloud to Mesh distance with Offset for Ouster6 (mm)

7. Conclusions

The paper provides an in-depth analysis of the accuracy and precision of indoor LiDAR systems, offering valuable insights into the factors influencing their performance. Utilizing a comprehensive dataset of unique LiDAR scans aligned with high-precision ground truth data, we demonstrated the variability in accuracy and precision across different LiDAR models. Key parameters such as sensor type, target material, and incident angle were identified as critical factors affecting measurement accuracy. Our results highlight the need for careful consideration of these factors when selecting and deploying LiDAR systems in robotics and autonomous applications.

The release of our dataset can serve as a benchmark for evaluating LiDAR performance and provides significant resources for developing future deep learning methods to better estimate and enhance LiDAR precision. The comprehensive metadata enables detailed analysis of LiDAR behavior across different materials, distances, and incident angles, facilitating more accurate sensor modeling and calibration techniques. It also contributes to the development of accurate SLAM and 3D reconstruction algorithms and may offer a benchmark for validating the accuracy of ICP algorithms in point cloud registration. Future work could involve the collection of more diverse datasets encompassing a broader range of indoor and outdoor environments. Investigating the performance of hybrid solid-state and solid-state LiDARs with different scanning patterns is another promising direction. Looking ahead, our efforts aim to push the limits of LiDAR accuracy, paving the way for broader applications in increasingly challenging environments. Developing automated methods to debias LiDAR scans based on identified error profiles is a potential avenue for future research.

Acknowledgements: This work has been partially funded by the Shanghai Frontiers Science Center of Human-centered Artificial Intelligence. The experiments of this work were supported by the core facility Platform of Computer Science and Communication, SIST, ShanghaiTech University.

References

[1] Ruslan Agishev, Tomáš Petříček, and Karel Zimmermann. Self-supervised depth correction of lidar measurements from map consistency loss. *IEEE Robotics and Automation Letters*, 8(8):4681–4688, 2023. 2

[2] Gerardo Atanacio-Jiménez, José-Joel González-Barbosa, Juan B Hurtado-Ramos, Francisco J Ornelas-Rodríguez, Hugo Jiménez-Hernández, Teresa García-Ramirez, and Ricardo González-Barbosa. Lidar velodyne hdl-64e calibration using pattern planes. *International Journal of Advanced Robotic Systems*, 8(5):59, 2011. 2

[3] Rene Bergelt, Owes Khan, and Wolfram Hardt. Improving the intrinsic calibration of a velodyne lidar sensor. In *2017 IEEE SENSORS*, pages 1–3. IEEE, 2017. 2

[4] Stefano Cattini, Davide Cassanelli, Luca Di Cecilia, Luca Ferrari, and Luigi Rovati. A procedure for the characterization and comparison of 3-d lidar systems. *IEEE Transactions on Instrumentation and Measurement*, 70:1–10, 2020. 2

[5] Ahmed Elaksher, Tarig Ali, and Abdullatif Alharthy. A quantitative assessment of lidar data accuracy. *Remote Sensing*, 15(2):442, 2023. 2

[6] FARO. Faro x330 datasheet. https://downloads.faro.com/index.php/s/Xgkc5nNaQZjc8ae?dir=undefined&openfile=41947, 2024. [Accessed 10-08-2024]. 3

[7] CL Glennie and PJ Hartzell. Accuracy assessment and calibration of low-cost autonomous lidar sensors. *The International Archives of the Photogrammetry, Remote Sensing and Spatial Information Sciences*, 43:371–376, 2020. 2

[8] Arsalan Haider, Yongjae Cho, Marcell Pigniczki, Michael H Köhler, Lukas Haas, Ludwig Kastner, Maximilian Fink, Michael Schardt, Yannik Cichy, Shotaro Koyama, et al. Performance evaluation of mems-based automotive lidar sensor and its simulation model as per astm e3125-17 standard. *Sensors*, 23(6):3113, 2023. 2

[9] Hesai. Hesai qt-64 datasheet. https://www.hesaitech.com/wp-content/uploads/PandarQT_User_Manual_Q01-en-240710.pdf, 2024. [Accessed 10-08-2024]. 3

[10] Hesai. Hesai xt-32 datasheet. https://www.hesaitech.com/wp-content/uploads/PandarXT_User_Manual_X01-en-240710.pdf, 2024. [Accessed 10-08-2024]. 3

[11] Ouster Inc. Ouster os0-128 rev6 datasheet. https://data.ouster.io/downloads/datasheets/datasheet-rev06-v2p5-os0.pdf, 2024. [Accessed 10-08-2024]. 3

[12] Ouster Inc. Ouster os0-128 rev7 datasheet. https://data.ouster.io/downloads/datasheets/datasheet-rev7-v3p1-os0.pdf, 2024. [Accessed 10-08-2024]. 3

[13] Misha Kazhdan, Ming Chuang, Szymon Rusinkiewicz, and Hugues Hoppe. Poisson surface reconstruction with envelope constraints. In *Computer graphics forum*, pages 173–182. Wiley Online Library, 2020. 5

[14] Carter Kelly, Benjamin Wilkinson, Amr Abd-Elrahman, Orlando Cordero, and H Andrew Lassiter. Accuracy assessment of low-cost lidar scanners: An analysis of the velodyne hdl–32e and livox mid–40's temporal stability. *Remote Sensing*, 14(17):4220, 2022. 2

[15] Bernhard Kerbl, Georgios Kopanas, Thomas Leimkühler, and George Drettakis. 3d gaussian splatting for real-time radiance field rendering. *ACM Trans. Graph.*, 42(4):139–1, 2023. 2

[16] Johann Laconte, Simon-Pierre Deschênes, Mathieu Labussière, and François Pomerleau. Lidar measurement bias estimation via return waveform modelling in a context of 3d mapping. In *2019 International Conference on Robotics and Automation (ICRA)*, pages 8100–8106. IEEE, 2019. 1, 2

[17] Jacob Lambert, Alexander Carballo, Abraham Monrroy Cano, Patiphon Narksri, David Wong, Eijiro Takeuchi, and Kazuya Takeda. Performance analysis of 10 models of 3d lidars for automated driving. *IEEE Access*, 8:131699–131722, 2020. 2

[18] Gyuseok Lee, Jangwoo Cheon, and Impyeong Lee. Validation of lidar calibration using a lidar simulator. *The International Archives of the Photogrammetry, Remote Sensing and Spatial Information Sciences*, 43:39–44, 2020. 2

[19] Alexander Millane, Zachary Taylor, Helen Oleynikova, Juan Nieto, Roland Siegwart, and César Cadena. C-blox: A scalable and consistent tsdf-based dense mapping approach. In *2018 IEEE/RSJ international conference on intelligent robots and systems (IROS)*, pages 995–1002. IEEE, 2018. 2

[20] Naveed Muhammad and Simon Lacroix. Calibration of a rotating multi-beam lidar. In *2010 IEEE/RSJ International Conference on Intelligent Robots and Systems*, pages 5648–5653. IEEE, 2010. 2

[21] H Nouiraa, Jean-Emmanuel Deschaud, and F Goulettea. Point cloud refinement with a target-free intrinsic calibration of a mobile multi-beam lidar system. *The International Archives of the Photogrammetry, Remote Sensing and Spatial Information Sciences*, 41:359–366, 2016. 2

[22] Optitrack. Optitrack prime 13 specs. https://optitrack.com/cameras/primex-13/specs.html, 2024. [Accessed 10-08-2024]. 3

[23] Kaustubh Pathak, Andreas Birk, Jann Poppinga, and Soren Schwertfeger. 3d forward sensor modeling and application to occupancy grid based sensor fusion. In *2007 IEEE/RSJ International Conference on Intelligent Robots and Systems*, pages 2059–2064, 2007. 2

[24] Ricardo Roriz, Jorge Cabral, and Tiago Gomes. Automotive lidar technology: A survey. *IEEE Transactions on Intelligent Transportation Systems*, 23(7):6282–6297, 2021. 1

[25] Na Sun, Quan Qiu, Zhengqiang Fan, Tao Li, Chao Ji, Qingchun Feng, and Chunjiang Zhao. Intrinsic calibration of multi-beam lidars for agricultural robots. *Remote Sensing*, 14(19):4846, 2022. 2

[26] Xin Wang, HuaZhi Pan, Kai Guo, Xinli Yang, and Sheng Luo. The evolution of lidar and its application in high precision measurement. In *IOP Conference Series: Earth and Environmental Science*, page 012008. IOP Publishing, 2020. 1

[27] Xiting Zhao and Sören Schwertfeger. 3dref: 3d dataset and benchmark for reflection detection in rgb and lidar data. In

2024 International Conference on 3D Vision (3DV), pages 225–234. IEEE, 2024. 4

[28] Qian-Yi Zhou, Jaesik Park, and Vladlen Koltun. Open3D: A modern library for 3D data processing. *arXiv:1801.09847*, 2018. 5